PCCP

PAPER

Disclosing the behavior under hydrostatic pressure of rhombohedral $MgIn_2Se_4$ by means of first-principles calculations†

Cite this: DOI: 10.1039/d0cp02842h

Khaled Boukri,[a] Tarik Ouahrani,*[ab] Michael Badawi,[c] Kamel Demmouche,[d] Ruth Franco[e] and J. Manuel Recio*[e]

Received 26th May 2020,
Accepted 3rd September 2020

DOI: 10.1039/d0cp02842h

rsc.li/pccp

AM_2X_4 crystalline materials display important technological electronic, optical and magnetic properties that are sensitive to general stress effects. In this paper, the behavior under hydrostatic pressure of the ambient condition rhombohedral phase of $MgIn_2Se_4$ is investigated in detail for the first time. We carried out first-principles calculations within the density functional theory framework aimed at determining the pressure-induced polymorphic sequence of this selenide. To accurately evaluate transition pressures at room temperature, thermal corrections have been included after the computation of phonon dispersion curves in potential candidate phases, namely the initial rhombohedral $R\bar{3}m$ one, inverse and direct spinels, $LiTiO_4$-type and defective $I\bar{4}$ structures. Only the transition from the $R\bar{3}m$ to the inverse spinel phase was found to fulfill the thermodynamic and mechanical stability criteria. The direct spinel could appear as metastable if kinetic effects hinder the above transition. Additionally, electronic band structures and chemical bonding properties were analyzed from the outcome of our quantum-mechanical solutions reporting band gap values and ionicity and noncovalent interaction indexes. It is shown that the investigated compound keeps behaving as a semiconductor, loses its van der Waals interactions, and becomes more covalent as hydrostatic pressure is applied.

1 Introduction

Structures with AM_2X_4 stoichiometry constitute a vast family of candidate materials for numerous applications[1–5] since they span a variety of interesting properties like ferro- and antiferromagnetism,[6] the coexistence of transparency and conductivity,[7] superconductivity,[8] and ferroelectricity.[9] Depending on the growth-temperature conditions,[10–13] these compounds emerge in different stable and metastable phases. For example, at a low growth-temperature, a cubic spinel and a hexagonal-type structure can coexist with this stoichiometry. In contrast, at high growth-temperature, orthorhombic and rhombohedral phases have been synthesized.[14] Instead of or combined with temperature, the application of hydrostatic pressure has also aroused great interest in both physics and chemistry communities. The effect of pressure at the gigapascal scale plays a significant role in the atomic and structural reorganization of these AM_2X_4 compounds, leading to an effective possibility of tailoring many innovative properties (ref. 14 and references therein).

Nevertheless, the difficulties are not negligible. Although transition paths and thermodynamic aspects are now computationally feasible to simulate (see for example ref. 15), a proposed mechanism and its corresponding energy profile are only one part within the kinetics realm of the transformation. In addition, a precise account of pressure/temperature ranges where one phase can be found to be metastable also needs a kinetic model involving the variable time. Other kinetic phenomena difficult to modelize are due for example to the non-equivalent transformations of single-crystal and powder samples or even to the coexistence of more than one phase over extended pressure ranges. This situation can lead to the appearance of different polymorphs depending on the time scale of the experiment where the sample is kept at a selected pressure. For all these reasons, phenomenological models and/or theoretical insights revealing when a metastable phase might emerge are always very valuable at guiding the

[a] Laboratoire de Physique Théorique, Université de Tlemcen, Tlemcen 13000, Algeria. E-mail: tarik_ouahrani@yahoo.fr; Tel: +213-43201824
[b] École supérieure en sciences appliquées, B.P. 165, Tlemcen 13000, Algeria
[c] Université de Lorraine and CNRS, LPCT, UMR 7019, 54506 Vandoeuvre-lés-Nancy, France
[d] Institut des Sciences, Centre Universitaire-Belhadj Bouchaib-Ain Temouchent, B.P. 284, 46000 Ain Temouchent, Algeria
[e] MALTA-Consolider Team and Departamento de Química Física y Analítica, Universidad de Oviedo, E-33006 Oviedo, Spain

† Electronic supplementary information (ESI) available. See DOI: 10.1039/d0cp02842h

pressure-based experiments and for an overall comprehension of the polymorphic sequence.

The rationalization of high-pressure phases in the AM_2X_4 crystal family requires a deep analysis of both its microscopic constituents and the observed polymorphs. At the experimental front, investigations on the behavior under extreme conditions of a number of such compounds with the AM_2X_4 stoichiometry have been reported for example in ref. 14 and 16–20. From the theoretical side, equations of state, and elastic and phonon dispersion calculations were carried out on a large number of cubic and non-cubic spinels as well as on post-spinel structures of these compounds (see the book of Manjón *et al.*[14]). Similar studies in Se-containing compounds were also performed by López-Moreno *et al.*[21] and Errandonea *et al.*[22] Most of these studies point out the crucial role played by the cation polyhedra and the disposition of occupied tetrahedral and octahedral interstices forming the unit cell of the specific material. However, an in-depth analysis of the relationship between the chemical structure and these atomic-level constituents is still needed. Such analysis can open ways for a better understanding of the effect of pressure on these compounds.

Using the quantum theory of atoms in molecules (QTAIM)[23] and basics of crystal chemistry,[24] it has been shown that the oxygen anions having a large volume are the main responsible constituents of the materials responding to hydrostatic pressure in oxide spinels.[25,26] However, when the unit cell volume is more equally shared between anions and cations, as in sulfur or selenide crystals with this stoichiometry, the atomic and bulk compressibilities may vary widely from one compound to another.[27,28] In previous work, and using these local analyses in the $MgIn_2S_4$ inverse spinel,[29] the calculation of the local (atomic) compressibilities identified the sulfur anion (similar to the oxygen anion in oxospinels) as the more affected by the application of hydrostatic pressure. In order to verify if the trend continues along with the chalcogenide group, it is worth exploring what the response is when S is replaced by Se keeping the same stoichiometry.

In this current study, we are interested in the selenide counterpart of the above compound of this family, namely $MgIn_2Se_4$. Contrary to $MgIn_2S_4$[29], which exhibits an intrinsic cation-disordered exchange between Mg^{2+} and In^{3+} at tetrahedral (tet) and octahedral (oct) sites, experimental evidence shows that $MgIn_2Se_4$ has a more complex structure. Its unit cell has a more random alternation of anions (Se) and cations (Mg and In) packed along the [001] direction, as well as a high concentration of antisite voids.[30,31] This characteristic gives birth to a layered sequence $(In)_{oct}$–$Se(In)_{tet}$–$Se(Mg)_{tet}$–$Se\cdots$–$Se(In)_{oct}$ of rhombohedral $R\bar{3}m$ symmetry, similar to that observed in $ZnIn_2S_4$.[32] This particular atomic organization favors many applications in the nano-structure field,[33] and motivates further experimental and theoretical studies on this compound, since they are almost non-existent and many of its properties are not yet well understood.

Overall, the aim of our contribution is two-fold. Firstly, we aim to fill the lack of data on this compound by characterizing its structural, bonding and electronic properties and quantifying them within the framework of density functional theory (DFT).[34–36] Secondly, we focus on the evaluation of the pressure effect on the rhombohedral structure of $MgIn_2Se_4$, with an emphasis on the eventual polymorphic sequence. To this end, along with standard solid state electronic structure methodologies, we will carry out atomic-level and chemical bonding analysis using QTAIM procedures and the noncovalent interaction (NCI)[37] approach. In this manner, we will extract pieces of information connecting the chemical-bonding pattern with the observed properties of the $MgIn_2Se_4$ compound.

Q4 Table 1 Crystallographic coordinates of atoms in the polymorphs of $MgIn_2Se_4$ explored in this work. The space group and the number of formula units (Z) are given. WP stands for the corresponding Wyckoff positions

Atom	WP	x	y	z	WP	x	y	z
Rombohedral ($R\bar{3}m$), Z = 3					Direct spinel ($Fd\bar{3}m$), Z = 8			
Mg1	3a	0.000	0.000	0.000	8a	0.12500	0.12500	0.12500
In1	6c	0.000	0.000	z	16d	0.50000	0.50000	0.50000
Se1	6c	0.000	0.000	z	32e	u	u	u
Se2	6c	0.000	0.000	z	—	—	—	—
Inverse spinel ($Imma$), Z = 4					$LiTiO_2$-type ($Imma$), Z = 4			
Mg1	4d	0.250	0.250	0.750	4c	0.250	0.250	0.250
In1	4b	0.000	0.000	0.500	4a	0.000	0.000	0.000
In2	4e	0.250	0.250	z	4d	0.250	0.250	0.750
Se1	8h	0.000	y	z	8h	0.000	y	z
Se2	8i	x	0.250	z	8i	x	0.250	z
Defective ($I\bar{4}$), Z = 2								
Mg1		2b		0.000		0.000		0.500
In1		2a		0.000		0.000		0.000
In2		2d		0.000		0.500		0.750
Se1		8g		u		u		u

The rest of the article is divided into three more sections. Next, we present the different structures of potential polymorph candidates of $MgIn_2Se_4$ and the computational details of our calculations. In the Results and discussion section, structure (including thermal effects and phonon dispersion curves), bonding and electronic band structure data are presented and analyzed for the stable and metastable polymorphs. The paper ends with a summary of our findings and conclusions.

2 Computational method

In order to clarify the presentation and discussion of our results, we present the unit cells of the rhombohedral, direct and inverse spinels, $LiTiO_2$-type, and defective polymorphs explored in this work in Table 1. Z stands for the number of formula units in the unit cell. Special and general Wyckoff positions are also given. Notice that taking into account both unit cell parameters and atomic coordinates, the total numbers of structural freedom degrees to be optimized in the calculations at each selected volume are 4 ($R\bar{3}m$), 1 ($Fd\bar{3}m$), 7 ($Immm$), 6 ($LiTiO_2$-type) and 2 ($I\bar{4}$). Fig. 1 displays a polyhedral view of the rhombohedral structure, while equivalent views for the rest of the polymophs are collected in Fig. S1 of the ESI.†

Our static calculations were performed using the plane-wave Vienna *ab initio* simulation package (VASP).[38,39] In order to consider both valence and the semi-core states, we have chosen the projector-augmented wave scheme (PAW)[40] implemented in this code. Thus, the valence electron-active space is constituted by, respectively, $2p^6\ 3s^2$, $3d^{10}\ 4s^2\ 4p^4$, and $4d^{10}\ 5s^2\ 5p^1$ for Mg, Se, and In atoms. Several parameterizations have been followed to treat the exchange and correlation potentials. Along with the standard local density (LDA)[41] and the generalized-gradient approximations *via* the Perdew–Burke–Ernzerhof functionals (GGA-PBE),[42] the semi-local functional GGA-PBEsol[43] was also tested to ensure the accuracy of the ground-state calculation. In addition, the Heyd–Scuseria–Ernzerhof (HSE) hybrid density functional (HSE06)[44] was specifically used to achieve an accurate description of the electronic band structures computed in this work. This functional has proved to perform better in the calculation of band gaps in semiconductors because it incorporates in its parametrization the short-range Hartree–Fock exchange interaction, while keeping a reasonable computational cost.[45] To optimize the layered $R\bar{3}m$ structure, van der Waals corrections to the total energy were taken into account by using the D3 method.[46,47] For consistency, this D3 correction was also introduced in the calculations of the other polymorphs. The plane-wave kinetic energy cutoff was tested and converged with a common value of 360 eV for all the polymorphs (see Fig. S2 in the ESI†). Also, we have used very dense reciprocal space sampling and Γ-centered Monkhorst–Pack meshes,[48] where the numbers of subdivisions along each reciprocal lattice vector $\vec{b}_i$ were given by $N_i = \max(1.30 \times |\vec{b}_i| + 0.5)$. To reduce computational costs, all the calculations were performed using primitive unit cells. Finally, the atomic relaxation was stopped when forces acting on atoms were less than 0.004 eV $Å^{-1}$ and the plane-wave kinetic energy cutoff is set to guarantee the total energy errors within 10^{-4} eV per formula unit in all the calculations. Computed energy-volume data points allows simulating the pressure response of the five polymorphs up to 10 GPa. This standard computational strategy allows geometry optimizations within the space groups of the selected structures, which are within the most common observed in this crystalline family. In order to introduce thermal effects, lattice-dynamics calculations were performed using generalized density-functional perturbation theory as implemented in the VASP and interfaced in the Phonopy package,[49] while the atomic Hellmann–Feynman forces are calculated with the VASP. This task requires the calculation of the ground state charge density and its linear response to external excitations.[50] The phonon frequencies are investigated in a $2 \times 2 \times 1$ supercell for the $R\bar{3}m$ structure and $2 \times 2 \times 2$ for the other ones.

In brief, the computational procedure starts by selecting a set of volumes per formula unit (V_i) where the structure of the corresponding polymorph was optimized by minimizing the formula unit crystalline energy (E_i). At a given pressure (p_j) and temperature (T_k), we add to the calculated (V_i,E_i) data set the p_jV_i term and the thermal contribution evaluated at the selected V_i values using the equations detailed in Section 3.1. Thus, we obtain (V_i,G_i) points for each polymorph at the chosen p_j and T_k conditions. G is the Gibbs energy that reduces to enthalpy H when temperature is neglected and to E if pressure is not considered. Numerical and analytical equations of state fitting to these calculated (V_i,H_i) and (V_i,G_i) data points were used to evaluate the corresponding equilibrium volumes and Gibbs energies. Chapters 1 and 2 of ref. 15 and 51 contain the details about this procedure.

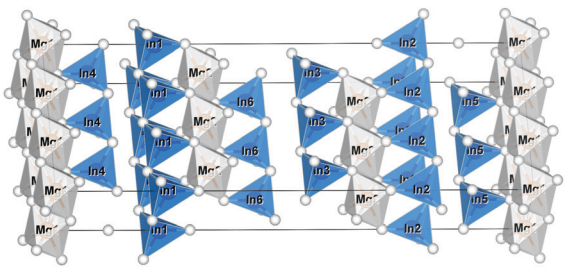

Fig. 1 Unit cell of the $MgIn_2Se_4$ $R\bar{3}m$ polymorph. Cation polyhedra with selenide (white spheres) at the corners display a layered structure along the c axis.

3 Results and discussion

3.1 Structure, equations of state, stability and phase transitions

The crystal growth measurements reported in ref. 30 conclude that $MgIn_2Se_4$ has a rhombohedral unit cell at zero pressure, with a quasi-layered form, crystalizing within the centrosymmetric space group $R\bar{3}m$ (point group $\bar{3}m$) as later reported in ref. 31 (see Fig. 1). The equilibrium geometry of this structure was calculated using three different computational levels, namely the LDA, the GGA-PBE, and the GGA-PBEsol. The effect

Table 2 Equation of state parameters of the investigated phases of $MgIn_2Se_4$ according to our calculations and other theoretical (Theor.) and experimental (Expt.) data

	a (Å)	b (Å)	c (Å)	(V_0/Z) (Å^3)	B_0 (GPa)	B_0'
Rhombohedral						
LDA	4.028	4.028	39.127	183.3	40.4	5.0
LDA+D3	4.010	4.010	38.705	179.7	42.7	5.7
GGA-PBE+D3	4.071	4.071	39.513	189.0	31.5	4.6
PBESol+D3	4.029	4.029	39.063	183.0	31.2	4.1
Expt.[31]	4.07(1)	4.07(1)	39.50(5)	188.883		
Expt.[30]	4.03	4.03	39.70	186.127		
Direct spinel						
LDA	11.325	11.325	11.325	181.6	67.4	4.7
LDA+D3	11.137	11.137	11.137	172.7	66.0	3.7
GGA-PBE+D3	11.309	11.309	11.309	180.8	57.3	4.5
Theor.[52]	11.43	11.43	11.43	186.66	60.97	
Inverse spinel						
LDA	7.552	7.668	10.542	172.6	62.9	3.5
LDA+D3	7.840	7.876	10.941	171.4	61.5	3.6
GGA-PBE+D3	7.992	8.032	11.190	179.6	58.0	4.8
$LiTiO_2$-Type						
LDA	7.438	7.532	10.442	146.3	52.4	4.6
LDA+D3	7.731	7.689	10.743	159.7	49.9	6.1
GGA-PBE+D3	7.846	7.810	10.889	166.8	47.9	5.1
Defective						
LDA	5.704	5.704	11.422	185.9	41.6	5.0
LDA+D3	5.687	5.687	11.382	184.0	35.8	5.2
GGA-PBE+D3	5.830	5.830	11.654	198.0	31.5	4.9

of the Grimme-D3 description of van der Waals (vdW) interactions was also explored. These data correspond to the so-called static approximation where the temperature is zero and zero-point vibrational contributions are neglected. These results are gathered in Table 2 along with the other four structures that will be discussed below. Our calculations indicate that the stable structure of $MgIn_2Se_4$ has the experimentally observed $R\bar{3}m$ space group (see Fig. 2).

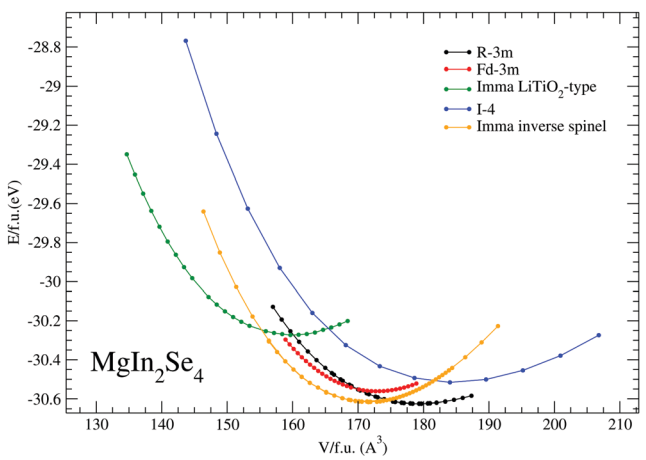

Fig. 2 Volume-dependence of the electronic energies of $MgIn_2Se_4$ for the $R\bar{3}m$ (a), *Imma* inverse spinel (b), $Fd\bar{3}m$ (c), *Imma* $LiTiO_2$-type (d), and $I\bar{4}$ (e) structures. Symbols stand for the calculated values, whereas the lines are a guide to the eye. All the values are for formula unit.

The comparison of the calculated values with the experimental lattice parameters and volume of the rhombohedral phase is quite good for the three levels of calculation, showing good agreement with respect to the more recent experimental data of Range,[31] and other theoretical calculations for the direct spinel[52] discussed below. D3 correction tends to slightly increase the cohesion of the crystal by decreasing the volume and lattice parameters. We have chosen the LDA+D3 approach to describe the rest of the properties, but explicit GGA-PBE+D3 results are also given in the main text and in the ESI.† The optimized z coordinates of In, Se1, and Se2 atoms are, respectively, 0.237 (0.237), 0.126 (0.127), and 0.300 (0.300) at the LDA+D3 level of calculation (in brackets are the GGA-PBE+D3 results), which also agree very well with the experimental values of Range[31] (0.234, 0.127, and 0.298, respectively). Crytallographic coordinates of atoms in general positions calculated at both LDA+D3 and GGA-PBE+D3 levels are gathered in Table S1 of the ESI† for all the polymorphs.

The evolution of the calculated electronic energy at the LDA+D3 level as a function of volume of the five structures explored in this work are shown in Fig. 2. A similar plot collecting E–V curves calculated at the GGA-PBE+D3 level is shown in Fig. S3 of the ESI.† Numerical and analytical (Vinet)[53] equations of state have been used to fit the calculated points providing the equilibrium volume (V_0), and bulk modulus (B_0) and its first pressure derivative (B_0'), all evaluated at zero pressure. LDA+D3 results pointed out that $MgIn_2Se_4$ in its layered stable phase at zero pressure has a small bulk modulus of around 43 GPa (31 GPa at GGA-PBE+D3), indicating that this phase is rather compressible as it should be for a structure dominated by van der Waals interactions.

It is worth noticing to compare the zero pressure bulk modulus obtained for the rest of the phases with the values obtained for other oxide and selenide spinels. Whereas many oxide spinels display B_0 values around 200 GPa[25,28] and a dependence of this property on the anion indicating a decreasing value to around 90–100 GPa for selenides,[27,28] our calculated value for the inverse spinel structure (62 GPa at LDA+D3 and 58 GPa at GGA-PBE+D3) is higher than that in the rhombohedral phase but lower than the suggested value for selenides with the spinel structure. Our values for the direct spinel are around 66 GPa (LDA+D3) and 57 GPa (GGA-PBE+D3), far from the expected value, thus showing that not only the anion but also the trivalent cation may quantitatively affect the compressibility of these spinel structures. Curiously, for the more open $I\bar{4}$ structure, the B_0 value of $CdCr_2Se_4$[27] and our computed values for $MgIn_2Se_4$ are very similar, around 40 GPa for the two compounds. To summarize pressure effects on the structure of all the polymorphs, we show in Fig. 3 how the volume and lattice parameters decrease in the 0–10 GPa range. All quantities are normalized with their corresponding values at zero pressure. Differences in the volume rates are fully consistent with the calculated B_0 values: direct and inverse spinels show the lowest rate, whereas the highest one is for the $I\bar{4}$ phase. In addition, the pressure-induced anisotropy is revealed to be not very important except for the rhombohedral phase

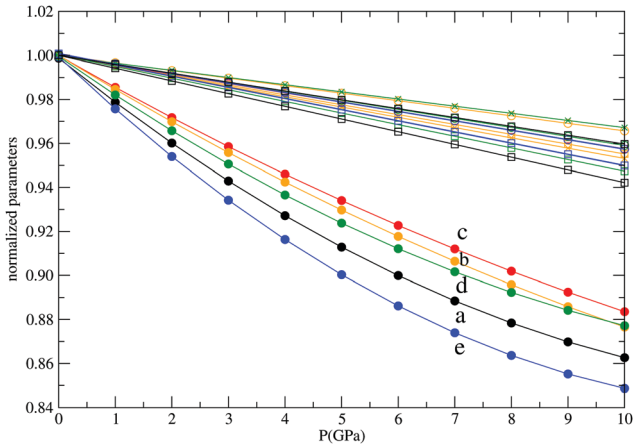

Fig. 3 Pressure evolution of normalized volume and lattice parameters for the $R\bar{3}m$ (a), *Imma* inverse spinel (b), $Fd\bar{3}m$ (c), *Imma* $LiTiO_2$-type (d), and $I\bar{4}$ (e), structures. Circles, crosses, and squares stand for a/a_0, b/b_0, and c/c_0, respectively.

that displays the expected greater compressibility along the *c* axis, which is about 1.5 times greater than that along the *a* axis.

In order to check the mechanical stability of $MgIn_2Se_4$ in the rhombohedral structure at zero pressure, phonon dispersion curves and phonon density of states were calculated. The spectrum is evaluated along the principal high symmetry directions throughout the $R\bar{3}m$ Brillouin zone. As the primitive unit cell of the rhombohedral $MgIn_2Se_4$ contains 7 atoms, one expects 21 vibrational modes, with three acoustic and 18 optical ones. Dispersion curves calculated at the LDA+D3 level are shown in Fig. 4, whereas the corresponding GGA-PBE+D3 curves are displayed in Fig. S4 of the ESI.† Table 3 collects the optical frequencies at the Γ-point calculated both at the LDA+D3 and GGA-PBE+D3 levels. Although the two figures and the tabulated values show an overall equivalent picture, we notice that there is a systematic blue shifting when the PBE functional is used, with differences being in general more important in the low-frequency range. The symmetry of the modes indicates which are Raman (g-type) and IR (u-type)

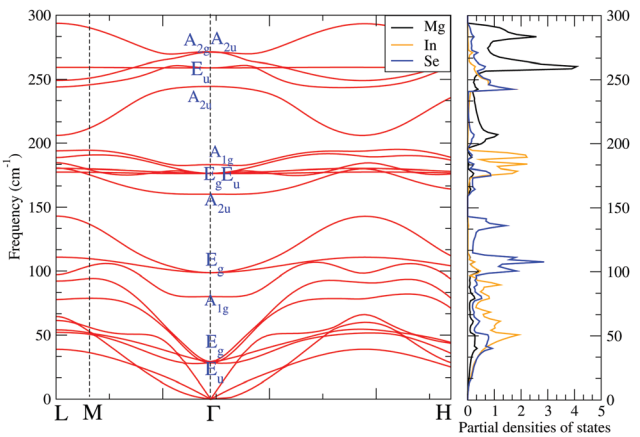

Fig. 4 Phonon dispersion and related partial density of states for $R\bar{3}m$ $MgIn_2Se_4$ at zero pressure according to our LDA+D3 calculations.

active. Unfortunately, we were not able to find any experimental data to compare with. The most important result from these calculations is that positive values are shown for all the phonon dispersion curves at both levels. This situation indicates that there are no imaginary frequencies and, therefore, we can confirm that $MgIn_2Se_4$ is mechanically stable in the $R\bar{3}m$ structure at zero pressure. Phonon density of states clearly shows that both Se and In species contribute to the acoustic and optical modes, at low frequencies. At high frequencies, the less weighted Mg anion contributes more to the optical branches. These calculations will be used later to add thermal effects to our static picture.

To predict the pressure range where one particular structure is thermodynamically stable at a given temperature, we have to calculate its Gibbs energy, $G(T,P)$, and compare its value with the values obtained for other potential candidates. In this work, we have considered up to five structures presented above (also gathered in Table 1) and explored a wide range of temperatures. In addition to the static $E + pV$ term, G contains a thermal contribution usually split into two terms F_{ZP} and F_{vib}:

$$F_{ZP} = \frac{\hbar}{2}\sum_{\mathbf{q},\nu}\omega_{\mathbf{q},\nu}(V), \quad (1)$$

$$F_{vib} = k_B T \sum_{\mathbf{q},\nu}\ln\left(1 - e^{-\frac{\hbar\omega_{\mathbf{q},\nu}(V)}{k_B T}}\right). \quad (2)$$

F_{ZP} refers to the zero point vibrational Helmholtz energy and F_{vib} to the pure vibrational contribution involved in the entropy term. $\omega_{\mathbf{q},\nu}$ stands for the calculated frequencies that depends on the particular acoustic or optical branch (ν) and the reciprocal space wavevector ($\mathbf{q}$), whereas k_B and $\hbar$ are, respectively, Boltzmann and Planck's constants. These expressions have been explicitly considered for the five polymorphs by the evaluation of the corresponding phonon dispersion curves in the first Brillouin zone in the framework of the quasi-harmonic approximation (QHA) at the LDA+D3 level. Under this approximation, anharmonicity is partially taken into account through the volume dependence of ω.

The thermodynamic equilibrium condition between two phases at a constant T and P is obtained when they reach the same $G(T,P)$ value. At that point, we define the transition temperature and pressure between the two phases, T_t and P_t, respectively. Thus, to determine P_t at a given temperature, the difference between the Gibbs energies of the two phases involved in the transformation has been calculated by adding F_{ZP} and F_{vib} (coming from our phonon calculations) to the previously computed electronic energies, E, of each structure and the corresponding pressure-volume term (pV). Alternatively, by plotting how the differences between the Gibbs energies of the phases explored in this work evolve as pressure is applied at different temperatures, we can determine P_t values (if any) from the crossing points between the curves describing the calculated points. Along with these very well-known criteria, we should emphasize that the thermodynamic transition data are not straightforwardly comparable with the observed values

Table 3 Vibrational frequencies in cm^{-1} at the Γ-point for the zero pressure $R\bar{3}m$ phase according to the LDA+D3 and GGA-PBE+D3 levels of calculation

Mode	E_u	E_g	A_{1g}	E_g	A_{2u}	E_g	A_{1g}	E_u	A_{2u}	E_u	A_{2u}	A_{1g}
LDA+D3	28.20	29.24	80.17	98.69	160.22	176.42	176.56	183.12	244.44	258.97	271.03	271.38
GGA-PBE+D3	75.11	87.69	112.90	119.83	172.92	198.61	198.61	199.43	265.91	270.15	281.32	290.98

in the laboratory (see for example Chapters 1 and 2 of ref. 15 for a thorough discussion of thermodynamic and kinetic computational and theoretical aspects of pressure-induced phase transitions). Due to energetic barriers associated with the transition, higher pressures (than P_t) are necessary. Kinetic effects control first-order pressure-induced transformations if the temperature is not very high, thus allowing other metastable phases to appear. Here, we focus on the thermodynamic realm, though some comments are also introduced regarding the potential presence of competitive metastable phases along the polymorphic sequence.

After evaluating the thermal contributions at 0 K and 300 K for the five structures, the corresponding Gibbs energies with respect to the zero pressure $R\bar{3}m$ stable phase at the same temperatures are displayed in Fig. 5. The defective $I\bar{4}$ phase was only computed at 0 K, since it is far from being a pressure-induced polymorph. Overall, the consideration of temperature effects on the phase stability at different pressure ranges is computationally very time-consuming and only phonon dispersion calculations have been carried out at the LDA level. Based on the calculated thermal contributions and the equivalent figure at static conditions at the GGA-PBE+D3 level (see Fig. S5 in the ESI†), we notice that the same conclusions can be drawn from both types of calculations.

Our results allow us to propose in principle two pressure-induced transformations. The sequence starts with a structural transformation at around 1 GPa from the rhombohedral $R\bar{3}m$ to the inverse spinel phase. This is a very competitive structure as can be also observed in Fig. 2. The difference in energy at zero pressure is less than 0.05 eV and its formula unit volume is ~8% lower than that of the rhombohedral one. The optimized atomic coordinates following the same order as in Table 1 are 0.138, 0.029, 0.747, 0.239, and 0.507.

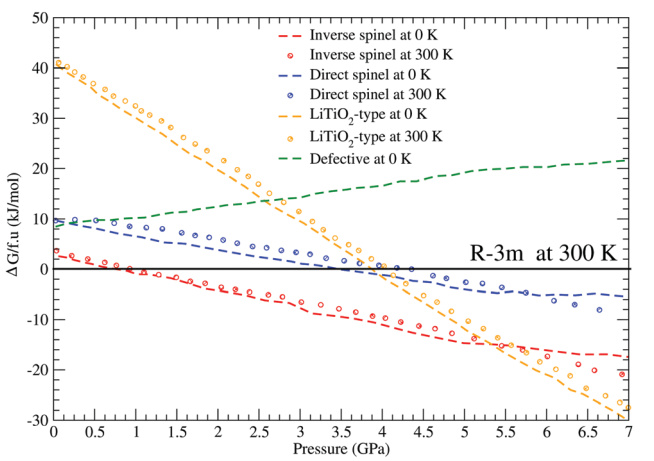

Fig. 5 Pressure-dependence of the Gibbs energy of $MgIn_2Se_4$ for the inverse spinel, direct spinel, $LiTiO_2$-type and defective structures with respect to the zero pressure $R\bar{3}m$ stable phase. Dotted and circular points display, respectively, calculated values at 0 K and 300 K at the LDA level. All the values are per formula unit.

According to the Gibbs energy diagram of Fig. 5, a second first-order transition to the $LiTiO_2$-type *Imma* phase could occur at ~5.5 GPa from the inverse spinel structure. The energy difference between this structure and the two previous ones is greater and around 0.5 eV at zero pressure. Its formula unit volume is around ~22% lower than that of the zero pressure rhombohedral stable phase. The calculated atomic coordinates for y and z of one Se atom, and x and z for the second one are, respectively, 0.993, 0.736, 0.245, and 0.499.

The polymorphic sequence derived from our LDA (Fig. 5) and GGA-PBE+D3 calculations (Fig. S5, ESI†) seem interesting compared with those transitions reported in a number of MgM_2X_4 compounds because, on one hand, the transformation leads to the loss of the vdW character of the compound and, and on the other hand, the polymorphic sequence differs from most of the first-order transitions reported for analogous compounds (ref. 14). Usually in pressure-induced phase transitions, the temperature does not affect the P_t values too much, at least in the low and intermediate-range.

To go further into the pressure-induced polymorphism, we would like to notice that, if the energetic barrier along the path from the $R\bar{3}m$ to the inverse spinel structure is high enough to hinder the transformation at a given temperature, then it could be possible to observe the direct spinel structure as a metastable phase at around 4 GPa or 5 GPa, respectively, depending on whether LDA or GGA-PBE+D3 calculations are considered. Looking at the corresponding G–P diagram, one can argue that the $LiTiO_2$-type phase could also emerge before the direct spinel, since at 300 K (LDA) and static conditions (GGA-PBE+D3) it has a lower Gibbs energy. However, the $LiTiO_2$-type structure has to be ruled out due to its mechanical instability, as we discuss in the following paragraphs. Fig. 2 shows that the direct spinel is already a competitive phase at zero pressure with an energy per formula unit only 0.2 eV higher than the rhombohedral structure and a volume ~4% lower than that of this phase. The optimized Se position is 0.259, within the range of values for this coordinate in many direct spinels.

For a complete assessment of the polymorphic sequence, it is convenient to check the mechanical stability of the new phases. We have first calculated the phonon dispersion curves for $R\bar{3}m$ at 1.5 GPa, inverse spinel at 2.5 GPa and cubic direct spinel at 5.0 GPa. The results (not plotted here for the sake of brevity, but included in Fig. S6–S8 of the ESI†) show that while

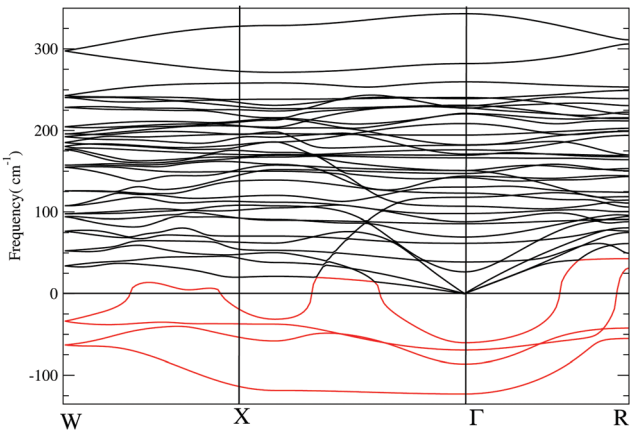

Fig. 6 Phonon dispersion plot of the *Imma* $LiTiO_2$-type phase of $MgIn_2Se_4$ at 5.5 GPa.

the phonon spectrum of $R\bar{3}m$ displays imaginary frequencies indicating a lattice instability at a pressure where this phase is not thermodynamically stable, the inverse *Imma* and direct $Fd\bar{3}m$ spinels are respectively mechanically stable at the calculated pressures where they are predicted to be stable and metastable, respectively.

Our second phonon dispersion calculations involve the predicted high-pressure *Imma* $LiTiO_2$-type phase. As revealed in Fig. 6, imaginary frequencies are found in wide regions of its first Brillouin zone at 5.5 GPa. The same result is obtained up to pressures of around 10 GPa. Although from the Gibbs energy calculations we can infer that $MgIn_2Se_4$ undergoes a transition at 5.5 GPa to the *Imma* $LiTiO_2$-type phase, the phonon study shows a mechanical instability of this phase, which has to be associated to the fact that in our optimizations constrains are imposed to keep the symmetry of the space group. Therefore, we conclude that this mechanical instability prevents the observation of the $LiTiO_2$-type at high pressures. Overall, these results contrast with the polymorphic sequence found in the sulfur $MgIn_2S_4$ counterpart.[14]

To summarize our phase stability analysis, just one pressure-induced phase transition from the rhombohedral to the inverse spinel structure is expected. However, due to kinetic effects, the direct spinel phase is not to be totally ruled out as pressure is applied in $MgIn_2Se_4$. The chance for this fact to occur should increase as temperature decreases, since at low tempertures the available vibrational energy to overcome the energy barrier between the rhombohedral and inverse spinel phases is lower. If this barrier is lower for the rhombohedral to the direct spinel structure, then we could observe this last phase at around 4 GPa. We also notice that the *Imma* $LiTiO_2$-type (which is mechanically unstable) and the $I\bar{4}$ structures cannot be accessed *via* hydrostatic pressure at least up to 10 GPa.

3.2 Bonding and interactions in $MgIn_2Se_4$

One can gain insight into the bonding properties of the $MgIn_2Se_4$ polymorphs by means of the topological analysis of the electronic density (ρ) following the Bader strategy.[23,54] The key point of this approach is the partition of the 3D real space of the unit cell into disjoint atomic basins (Ω), and then quantify the volume and electron population of each basin.[55] Our results in the layered $R\bar{3}m$ structure (see Table 4) show that the charges associated with Mg, In and the two non-equivalent Se atoms are, respectively, +1.67, +1.26, −0.88 and −1.21, far from the pure ionic values. By simply adding the ratios of these effective charges ($\mathcal{Q}(\Omega)$) with respect to the corresponding nominal oxidation states ($\mathscr{L}(\Omega)$) for the N atoms of the formula unit, we evaluate an index that measures the degree of ionicity of this structure:[56] $\alpha = \frac{1}{N}\sum_{\Omega=1}^{N}\frac{\mathscr{L}(\Omega)}{\mathrm{OS}(\Omega)} = 53.79\%$.

Table 4 QTAIM partition of the equilibrium $R\bar{3}m$ unit cell of $MgIn_2Se_4$ at zero pressure. M stands for the atom multiplicity, V_i for the atomic volume in atomic units, Q is the atomic charge, and CT is the charge transferred

Atom	Z	M	V_i	Q (e)	CT (%)
Mg	8	3	72.59	1.668	83.40
In	13	6	206.72	1.255	40.83
Se1	6	6	196.09	−0.876	43.80
Se2	6	6	198.56	−1.213	60.65

In contrast to the $MgIn_2S_4$ compound with a value of α = 79%, the lower value in the $R\bar{3}m$ structure suggests an important mixing of covalent and ionic contributions to its bonding network. If we compare the degree of ionicity with the other stable phases, we find that the inverse spinel one has α = 43% and the direct spinel has 44%. We also noticed that the ionicity increases weakly as pressure is applied in the rhombohedral phase from 0 to 4 GPa, which means that the charge transferred from the metallic atoms (Mg and In) to Se increases as pressure is applied. As regards the distribution of the atomic volumes, it is interesting to notice that there is not a clear dominance of the anion size as in oxide spinels. The fact that both, In and Se, show similar atomic volumes might explain in part why the B_0 values for the $MgIn_2Se_4$ spinel structures present lower values than the ones suggested for selenide spinels (see the discussion above).

Given the importance of the weak vdW interactions in holding together the layers in the low-pressure $R\bar{3}m$ structure, it is also very informative to evaluate maps of the so-called reduced gradient of the electron density (s). These maps reveal regions controlled by non-covalent interactions (NCI)[37] where both ρ and s have low values. We can estimate the strength of NCIs by specifying the range of interactions by color attribution:[57] blue for attractive interactions, red for the repulsive or closed-shell ones and, finally, van der Waals (vdW) contacts by green color.

According to the plot displayed in Fig. 7, we can see that even if we take an isovalue for s = 0.5, the isosurface regions show a dominance of the van der Waals interactions, which are delocalized, and correspond to the contacts between layers. Also, the ionic (in red) and covalent bonds (in blue) do not seem very pronounced. However, the strong interactions in blue color and repulsive ones are very localized, so that their 3D surfaces

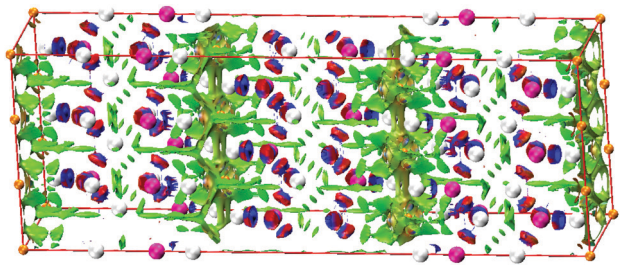

Fig. 7 NCI isosurfaces of the $R\bar{3}m$ phase of $MgIn_2Se_4$. Surfaces are colored in the [−0.04, 0.04] a.u. range of (sign(λ_2)ρ(**r**)) (isovalue s = 0.5 a.u.). Repulsive interactions are shown as red isosurfaces, van der Waals interactions as thin, delocalized green regions, and strong attractive interactions as localized blue lentils.

are compact. The density accumulations between In cations and Se anions are very small, and for this reason, they appear as disc-shaped surfaces or as thin surfaces around the bond critical point.

3.3 Electronic band structure calculations

Once the structural changes and bonding analysis under pressure have been discussed, we extend our study to the electronic band structures of the stable and metastable $MgIn_2Se$$MgIn_2Se_4$ polymorphs. To do that, the HSE06 hybrid functional has been

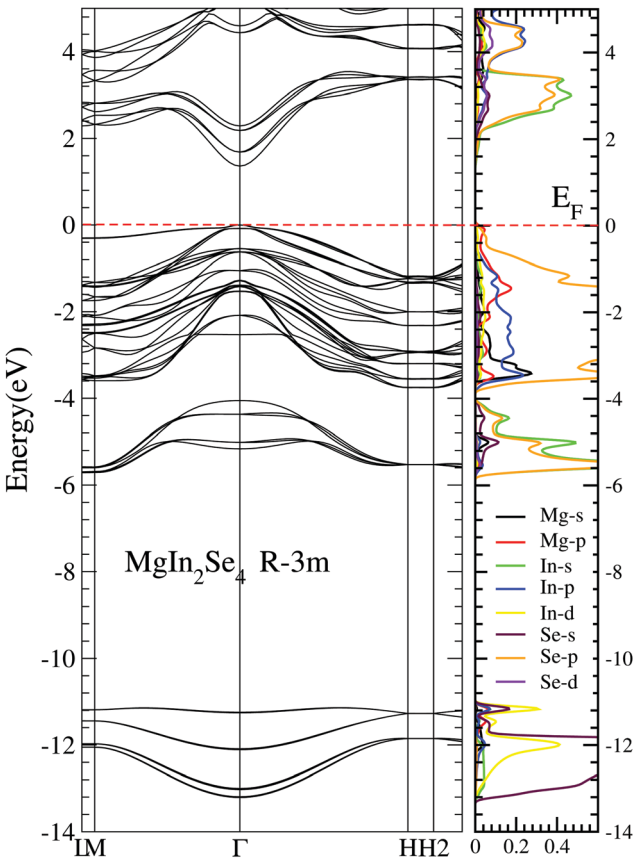

Fig. 8 Zero pressure calculated band structure of the $R\bar{3}m$ phase of $MgIn_2Se_4$.

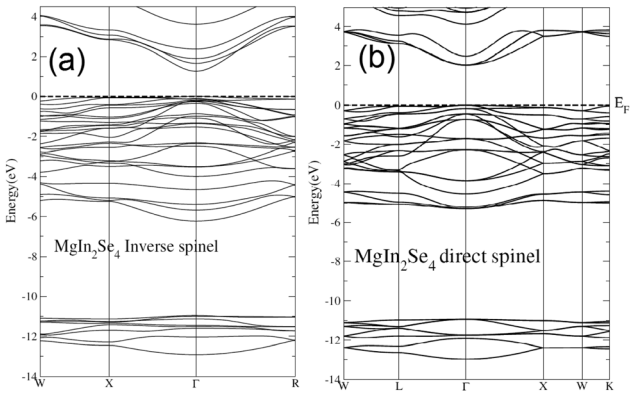

Fig. 9 Calculated band structure of the of $MgIn_2Se_4$ compound, (a) the inverse spinel phase at 1.5 GPa and (b) the direct spinel phase at 2.5 GPa.

used in our calculations with the aim of determining the value and nature of the bandgap and how it changes with pressure and across the transitions. To illustrate our results, the band structures of the three phases are presented in Fig. 8 and 9. Pressures are different and correspond to the equilibrium structures found at zero pressure ($R\bar{3}m$), 1.5 GPa (inverse spinel) and 2.5 GPa (direct spinel). The overall picture is fairly similar in the three polymorphs with a narrow region centered around −12 eV (mainly dominated by Mg 2p orbitals), a valence band from around −6 eV to the Fermi level (the top dominated by Se 4p-like orbitals) and the conduction band starting around 2 eV (the bottom dominated by In 5s-like orbitals).

As concerns the nature of the bandgap, the three structures show that it is direct and located at the Γ point. The value of the bandgap decreases when going from the layered $R\bar{3}m$ low-pressure phase (1.37 eV) to the inverse spinel structure (1.27 eV) and then increases in the cubic direct spinel (2.00 eV). It seems that the transposition of cations from tetrahedral to octahedral sites caused by the phase transition to the $Fd\bar{3}m$ structure affects the nature of bonding interactions. The calculated band gap of this phase (2 eV) is very close to the one reported (1.9 eV) in ref. 52 using a different level of calculation. We should notice that both our LDA and GGA-PBE calculations, yield band gap values too low at their corresponding zero pressure equilibrium volumes for the rhombohedral, inverse, and direct spinels, respectively, validating the choice of the hybrid HSE06 functional. For the three phases, we obtain greater band gap values as pressure increases (see also Fig. S9

Table 5 Band gap values (E_g) for different pressures for the $R\bar{3}m$, inverse, and direct phases of $MgIn_2Se_4$. All data are calulated at the HSE06 level except zero pressure values in the second (LDA+D3) and third row (GGA-PBE+D3). E_g and P in eV and GPa, respectively

P	$R\bar{3}m$	Inverse	Direct
0 (HSE06)	1.37	1.14	1.99
0 (LDA+D3)	0.46	0.28	1.03
0 (GGA-PBE+D3)	0.53	0.13	0.70
1.5	1.46	1.27	2.00
2.5	1.55	1.33	2.00
4.0	1.66	1.50	2.03

in the ESI†). Similar behavior was found for the zero pressure structure of the oxospinel $CdAl_2O_4$.[58] Despite the importance of $MgIn_2Se_4$ polymorphs in the fabrication of optical devices, to the best of our knowledge, no data were found in the literature concerning the measure of its bandgap. So, we consider that our findings may motivate further experimental investigations on this material (Table 5).

4 Conclusions

The stability of $MgIn_2Se_4$ under hydrostatic pressure has been deeply investigated for the first time by means of standard quantum mechanical solid state electronic structure methodologies involving also phonon dispersion curve calculations to account for thermal effects. Up to five potential structures commonly observed in AM_2X_4 materials were considered. A rhombohedral layered $R\bar{3}m$ phase was found to be the thermodynamically stable one at ambient conditions. This result and the subsequent structural characterization are in very good agreement with the reported equilibrium experimental data.[31] The chemical bonding network of the rhombohedral phase presents an in-layer mixing of ionic-covalent character along with vdW weak interactions holding the layers together according to our QTAIM and NCI analysis. This allows us to explain the high compressibility of this structure. On the other hand, the two spinel phases show greater bulk moduli but lower than those expected for selenides according to previous studies.[27,28] This result might be understood as due to the equally shared space occupied by In and Se in this particular compound.

We predict a pressure-induced phase transition from the $R\bar{3}m$ phase to an inverse spinel structure at $\sim$1 GPa and 300 K. Although a $LiTiO_2$-type phase is evaluated with the same Gibbs energy as the inverse spinel structure at $\sim$5.5 GPa, the phonon dispersion curves computed for the $LiTiO_2$-type phase at the same pressure and at 10 GPa show imaginary frequencies, thus detecting a mechanical instability for this orthorhombic phase that has to be ruled out in the polymorphic sequence. On the other hand, a direct spinel structure may appear as a metastable phase around 4 GPa in spite of having higher Gibbs energy than the inverse spinel one. This possibility increases at low temperatures, since the energetic barrier connecting the rhombohedral and inverse spinel structures could be high enough to be overcome with the available vibrational energy at low T. Additionally, our endeavor provides results on the effect of pressure on the electronic properties of the stable and metastable phases of $MgIn_2Se_4$. All of them show direct bandgaps, with values of 1.37 eV (rhombohedral), 1.14 eV (inverse spinel) and 1.99 eV (direct spinel), which an increase slightly as pressure is applied in correspondence with a greater charge transfer from the cations to the selenide atoms. Overall, the reported properties and behavior of the layered ambient condition-stable structure of $MgIn_2Se_4$ suggest that this material could be very promising for photovoltaics/catalysis applications.

Conflicts of interest

Acknowledgements

Financial support is from MCIU, Principado de Asturias-FICYT, and FEDER (projects PGC2018-094814-B-C22, FC-GRUPIN-IDI/2018/000177, RED2018-102612-T) and GENCI-CCRT (Grants No. A0080910433). We would like to thank the PMMS (Pôle Messin de Modélisation et de Simulation) and the MALTA-Consolider computational facilities for providing us with the computational resources.

References

1 G. Gusmano, G. Montesperelli, E. Traversa and G. Mattogno, *J. Am. Ceram. Soc.*, 1993, **76**, 743.
2 A. Govindaraj, E. Flahaut, C. Laurent, A. Peigney, A. Rousset and C. N. R. Rao, *J. Mater. Res.*, 1999, **14**, 2567.
3 N. J. Van der Laag, *Environnemental effects on the fracture of oxide ceramics*, *Doctorat thesis*, Technical University, Eindhoven, 2002.
4 X. Liu, H. Wang, B. Lavina, B. Tu, W. Wang and Z. Fu, *Inorg. Chem.*, 2014, **53**, 5986–5992.
5 T. Irifune, K. Fujino and E. Ohtani, *Nature*, 1991, **349**, 409.
6 N. W. Grimes, *Phys. Technol.*, 1975, **6**, 22.
7 M. Dekkers, G. Rijnders and D. H. A. Blank, *Appl. Phys. Lett.*, 2007, **90**, 021903.
8 J. Akimoto, Y. Gotoh, K. Kawaguchi and Y. Oosawa, *J. Solid State Chem.*, 1992, **96**, 446.
9 Y. Yamasaki, S. Miyasaka, Y. Kaneko, J. P. He, T. Arima and Y. Tokura, *Phys. Rev. Lett.*, 2006, **96**, 207204.
10 M. E. Hills, D. C. Harris and C. K. Lowe-Ma, *J. Phys. Chem. Solids*, 1987, **48**, 501–507.
11 H. J. Berthold and K. Köhler, *Z. Anorg. Allg. Chem.*, 1981, **475**, 45–49.
12 K. T. Kaifuku, I. Aksenov and K. Sato, *Jpn. J. Appl. Phys.*, 1995, **34**, 3073–3074.
13 N. A. Moldovyan, M. N. Markus and S. I. Radautsan, *Dokl. Akad. Nauk USSR*, 1989, **304**, 151–155.
14 F. J. Manjón, I. Tiginyanu and V. Ursaki, *Pressure-Induced Phase Transitions in AB_2X_4 Chalcogenide Compounds,* Springer Heidelberg, New York Dordrecht London, 2014.
15 *An Introduction to High-Pressure Science and Technology*, ed. J. M. Recio, J. M. Menendez and A. Otero-de-la-Roza, CRC-Press, Boca Raton, FL, USA, 2016.
16 S. Asbrink, A. Waskowska, J. S. Olsen and L. Gerwand, *Phys. Rev. B: Condens. Matter Mater. Phys.*, 1998, **57**, 4972–4974.
17 I. Efthimiopoulos, T. Lochbiler, V. Tsurkan, A. Loidl, V. Felea and Y. Wang, *J. Phys. Chem. C*, 2017, **121**, 769–777.
18 D. Errandonea, R. S. Kumar, F. J. Manjón, V. V. Ursaki and E. V. Rusu, *Phys. Rev. B: Condens. Matter Mater. Phys.*, 2009, **79**(6), 024103.
19 S.-H. Wei and S. B. Zhang, *Phys. Rev. B: Condens. Matter Mater. Phys.*, 2001, **63**, 045112.

20 G. Döll, M. Ch Lux-Steiner, Ch Kloc, J. R. Baumann and E. Bucher, *J. Cryst. Growth*, 1990, **104**, 593.

21 S. López-Moreno, D. Errandonea, P. Rodriguez-Hernandez and A. Muñoz, *Inorg. Chem.*, 2015, **54**, 1765.

22 D. Errandonea, A. Muñoz, P. Rodriguez-Hernandez, J. E. Proctor, F. Sapiña and M. Bettinelli, *Inorg. Chem.*, 2015, **54**, 7524.

23 R. F. W. Bader, *Atoms in molecules: A quantum theory*, Clarendon Press, Oxford, UK, 1990, p. 438.

24 R. M. Hazen and L. W. Finger, *Comparative Crystal Chemistry: Temperature, Pressure, Composition and the Variation of Crystal Structure*, Wiley, 1 edn, 1982.

25 J. M. Recio, R. Franco, A. Martín Pendás, M. A. Blanco, L. Pueyo and R. Pandey, *Phys. Rev. B: Condens. Matter Mater. Phys.*, 2001, **63**, 184101.

26 A. Martín Pendás, A. Costales, M. A. Blanco, J. M. Recio and V. Luaña, *Phys. Rev. B: Condens. Matter Mater. Phys.*, 2000, **62**, 13970.

27 A. Waśkowska, L. Gerward, J. Staun Olsen, M. Feliz, R. Llusar, L. Gracia, M. Marqúes and J. M. Recio, *J. Phys.: Condens. Matter*, 2004, **16**, 53.

28 L. Gerward, J. Z. Jiang, J. Staun Olsen, J. M. Recio and A. A. Waśkowska, *J. Alloys Compd.*, 2005, **401**, 11–17.

29 S. Belarouci, T. Ouahrani, N. Benabdallah, Á. Morales-García and R. Franco, *Phase Transitions*, 2018, **91**, 759–771.

30 L. Gastaldi, A. Maltese and S. Viticoli, *J. Cryst. Growth*, 1984, **66**, 673–675.

31 K.-J. Range, *Z. Naturforsch., B: J. Chem. Sci.*, 1996, **51**, 1363–1364.

32 S. A. Lopez-Rivera, A. J. Mora, D. Acosta Najarro, A. V. Rivera and R. Avila Godoy, *Semicond. Sci. Technol.*, 2001, **16**, 367–371.

33 F.-D. Yu, L.-F. Que, Z.-B. Wang, Y. Zhang, Y. Xue, B.-S. Liua and D.-M. Gua, *J. Mater. Chem. A*, 2016, **4**, 18416–18425.

34 J. Srour, M. Badawi, F. E. H. Hassan and A. V. Postnikov, *Phys. Status Solidi B*, 2016, **253**, 1472–1475.

35 J. Srour, M. Badawi, F. El Haj Hassan and A. Postnikov, *J. Chem. Phys.*, 2018, **149**, 054106.

36 T. Ayadi, L. Debbichi, M. Badawi, M. Said, H. Kim, D. Rocca and S. Lebague, *Phys. E*, 2019, **114**, 113582.

37 E. R. Johnson, S. Keinan, P. Mori-Sánchez, J. Contreras-García, A. J. Cohen and W. Yang, *J. Am. Chem. Soc.*, 2010, **132**, 6498–6506.

38 G. Kresse and J. Hafner, *Phys. Rev. B: Condens. Matter Mater. Phys.*, 1993, **47**, 558–561.

39 G. Kresse and J. Furthmüller, *Comput. Mater. Sci.*, 1996, **6**, 15–50.

40 P. E. Blöchl, *Phys. Rev. B: Condens. Matter Mater. Phys.*, 1994, **50**, 17953–17979.

41 J. R. Perdew and Y. Wang, *Phys. Rev. B: Condens. Matter Mater. Phys.*, 1992, **45**, 13244–13249.

42 J. P. Perdew, K. Burke and M. Ernzerhof, *Phys. Rev. Lett.*, 1996, **77**, 3865.

43 J. P. Perdew, A. Ruzsinszky, G. I. Csonka, O. A. Vydrov, G. E. Scuseria, L. A. Constantin, X. Zhou and K. Burke, *Phys. Rev. Lett.*, 2000, **100**, 136406.

44 J. Heyd, G. E. Scuseria and M. Ernzerhof, *J. Chem. Phys.*, 2003, **118**, 8207.

45 A. J. Garza and G. E. Scuseria, *J. Phys. Chem. Lett.*, 2016, **7**, 4165.

46 S. Grimme, J. Antony, S. Ehrlich and S. Krieg, *J. Chem. Phys.*, 2010, **132**, 154104.

47 S. Grimme, S. Ehrlich and L. Goerigk, *J. Comput. Chem.*, 2011, **32**, 1456.

48 H. J. Monkhorst and J. D. Pack, *Phys. Rev. B: Condens. Matter Mater. Phys.*, 1976, **13**, 5188–5192.

49 A. Togo, F. Oba and I. Tanaka, *Phys. Rev. B: Condens. Matter Mater. Phys.*, 2008, **78**, 134106.

50 S. Baroni, S. de Gironcoli, A. Dal Corso and P. Gianozzi, *Rev. Mod. Phys.*, 2001, **73**, 515.

51 A. Otero-de-la-Roza, D. Abassi-Pérez and V. Luaña, *Comput. Phys. Commun.*, 2011, **182**, 2232–2248.

52 Q. Mahmood, M. Rashid, N. N. A. Qurat-Ul-Ain, M. G. Bahar Ashiq, M. S. Ramay and A. Mahmood, *J. Mol. Graphics Modell.*, 2019, **88**, 168–173.

53 P. Vinet, J. H. Rose, J. Ferrante and J. R. Smith, *J. Phys.: Condens. Matter*, 1989, **1**, 1941–1963.

54 T. Ouahrani, A. Otero de-la Roza, A. H. Reshak, R. Khenata, H. I. Faraoun, B. Amrani, M. Mebrouki and V. Luaña, *Phys. B*, 2010, **405**, 3658–3664.

55 A. Otero-de-la-Roza, E. R. Johnson and V. Luaña, *Comput. Phys. Commun.*, 2014, **185**, 1007–1018.

56 P. Mori-Sánchez, A. Martín Pendás and V. Luaña, A classification of covalent, ionic, and metallic solids based on the electron density, *J. Am. Chem. Soc.*, 2002, **124**, 14721.

57 R. A. Boto, J. P. Piquemal and J. Contreras García, *Theor. Chem. Acc.*, 2017, **136**, 139.

58 A. Bouhemadou, F. Zerarga, A. Almuhayya and S. Bin-Omran, *Mater. Res. Bull.*, 2011, **46**, 2252–2260.